Title of the dissertation

A DISSERTATION PRESENTED
BY
MATTHEW N. RISPOLI
TO
THE DEPARTMENT OF PHYSICS

IN PARTIAL FULFILLMENT OF THE REQUIREMENTS
FOR THE DEGREE OF
DOCTOR OF PHILOSOPHY
IN THE SUBJECT OF
PHYSICS

HARVARD UNIVERSITY
CAMBRIDGE, MASSACHUSETTS

MAY 2019

Thesis advisor: Professor Markus Greiner Matthew N. Rispoli

Title of the dissertation

Abstract

Lorem ipsum dolor sit amet, consectetuer adipiscing elit. Morbi commodo, ipsum sed pharetra gravida, orci magna rhoncus neque, id pulvinar odio lorem non turpis. Nullam sit amet enim. Suspendisse id velit vitae ligula volutpat condimentum. Aliquam erat volutpat. Sed quis velit. Nulla facilisi. Nulla libero. Vivamus pharetra posuere sapien. Nam consectetuer. Sed aliquam, nunc eget euismod ullamcorper, lectus nunc ullamcorper orci, fermentum bibendum enim nibh eget ipsum. Donec porttitor ligula eu dolor. Maecenas vitae nulla consequat libero cursus venenatis. Nam magna enim, accumsan eu, blandit sed, blandit a, eros.

Quisque facilisis erat a dui. Nam malesuada ornare dolor. Cras gravida, diam sit amet rhoncus ornare, erat elit consectetuer erat, id egestas pede nibh eget odio. Proin tincidunt, velit vel porta elementum, magna diam molestie sapien, non aliquet massa pede eu diam. Aliquam iaculis. Fusce et ipsum et nulla tristique facilisis. Donec eget sem sit amet ligula viverra gravida. Etiam vehicula urna vel turpis. Suspendisse sagittis ante a urna. Morbi a est quis orci consequat rutrum. Nullam egestas feugiat felis. Integer adipiscing semper ligula. Nunc molestie, nisl sit amet cursus convallis, sapien lectus pretium metus, vitae pretium enim wisi id lectus. Donec vestibulum. Etiam vel nibh. Nulla facilisi. Mauris pharetra. Donec augue. Fusce ultrices, neque id dignissim ultrices, tellus mauris dictum elit, vel lacinia enim metus eu nunc.

Contents

This is the dedication.

Acknowledgments

Short thank yous

Are we still having fun?

Dr. Daniel Greif

0 Introduction

Punchy very general intro about quantum simulation, correlated systems, and intractable problems

We have developed a wildly successfful microscopic theory of the universe via quantum mechanics (no, it doesn't seem to quite capture everything, but it's remarkably good) and we also have a very comfortable intuitive set of macroscopic phenomena we all know, love, and experience on a daily basis. Can these things become compatable?

Emphasize the difference between larger, more particles and the every day world which is an open-system.

The key here maybe be in how information and correlations develop, something that requires an intense amount of tunability and versatility in an experimental apparatus. In walks the QGM where we have access to an unprecedented amount of information and can, for example, capture all spatial correlations in a wave-function.

1

Optical Lattices and the Bose-Hubbard model

1.1 Single-particle physics in optical lattices

Ultra-cold neutral atoms in optical lattices provide a new paradigm in the ability to experimentally simulate quantum models. The level of control that can be applied to manipulating atoms enables physicists to realize truly quantum phenomena with level of high precision. In this work, we will ... T, why they're special and some arguments about deBroglie wavelength. We have very clean systems unlike most real materials. What about when we apply disorder?

Optical electronic transitions in neutral atoms provide both conservative forces and dissipative forces (metcalf). These two processes can be thought of as elastic and inelastic scattering, respectively, of photons with the atom. The dissipative force is provided by the absorption of a photon or emission of a photo and has been famously used for trapping and cooling of atomic gases. However, the vast majority of all work or models discussed in this thesis will rely on tailoring conservative potentials with almost arbitrary spatial control. Since the only external forces that interact with the atoms are predominantly conservative, the system remains, to a very good approximation, isolated from the surrounding external environment.

1.1.1 Neutral atoms in optical potentials

A neutral atom experiences a conservative external potentials from optical photons when the light the atom interacts with is far from resonance. This light, rather than being absorbed by the atom, induces an electric dipole moment in the atom. The amplitude of the alignment, or anti-alignment, of this dipole moment with the external electrical field changes the energy of the atom and is known as

the ac-Stark shift. In the case of a two level atom in a monochromatic laser field, where the laser detuning is large enough that the rotating wave approximation can be used, the conservative potential provided by the dipole atom-light interaction is given by:

$$V_{dipole}(r) \approx \frac{3\pi c^2}{2\omega_o^3}\frac{\Gamma}{\Delta}I(r) \tag{1.1}$$

where the atomic transition frequency is ω_o, the linewidth of the transition is Γ, the intensity of the laser power is $I(r)$, and the detuning of the laser frequency from the atomic transition is $\Delta = \omega - \omega_o$. Note that the both the laser intensity, $I(r)$, and the detuning, Δ, are complimentary ways to change dipole potential depth. Additionally, the sign of the detuning Δ controls whether the atom is attracted to or repelled from the high-intensity locations of the laser beam profile. This is commonly referred to as either red- or blue-detuning of the laser with respect to the atomic transition frequency due to their relationship of the colors in the visible spectrum. While (1.1) is written for a two level atom approximation, additional energy levels can be included to provide a more accurate response (cite someone).

However, the laser illuminating the atom does not act purely as a conservative potential since the photons can exchange energy with the the atom by exciting an electron to an excited state. The likelihood of such a dissipative process depends on both the intensity of the light, I and the laser detuning with respect to the linewidth of the atomic transition Γ/Δ. The rate at which an atom scatters light is given by (1.2).

$$\Gamma_{sc}(r) \approx \frac{3\pi c^2}{2\hbar\omega_o^3}\left(\frac{\Gamma}{\Delta}\right)^2 I(r) = \frac{1}{\hbar}\frac{\Gamma}{\Delta}V_{dipole}(r) \tag{1.2}$$

By detuning the laser far from resonance, we see that the scattering rate, or dissipative contribution of the light-atom interaction, is reduced compared to the conservative contribution by a factor of (Γ/Δ). This implies that for the same desired dipole potential depth V_o, it is always favorable to increase both the laser detuning and the intensity to reduce the scattering rate to more faithfully realize a purely conservative potential.

This consideration of these two scalings provide some guidance in how to choose practical parameters for the lasers that produce the desired optical potentials. In the case of ^{87}Rb, the two relevant optical transitions come from the D1 and D2 lines of the $5s \rightarrow 6p$ transition which occur at $\lambda = 795$nm and $\lambda = 780$nm respectively. All attractive, red-detuned, potentials in this work are derived from a broadband $\lambda \approx 840$nm SLED source*. All repulsive, blue-detuned, potentials are derived from a similar broadband $\lambda \approx 758$nm SLED source†. We will predominantly study Hamiltonians provided purely by this repulsive light.

1.1.2 Bandstructure and Bloch wavefunctions

All experiments in this thesis will be realized in an effective 1-D optical lattice that is generated from interfering the blue detuned light. The potential generated from this light depends on the intensity of its interference pattern and is written as:

*EXALOS bladdy blue
†EXALOS bladdy blue2

$$V(x) = -(V_o/2)\cos(2kx) \tag{1.3}$$

where k [‡] is the wavevector (or k-vector) of the light used to create the potential and m is the mass of the atom. The potential has been written with no dc-potential offset for convenience. The total Hamiltonian then for a single-particle is written as:

$$H = \frac{\hat{p}^2}{2m} + V(x) \tag{1.4}$$

In the case of zero lattice depth, V_o, this Hamiltonian realizes a single-particle in free space whose eigenstates are described by a propagating wave with an eigenenergy that depends only on its momentum $\hbar k$: $\psi_k = e^{ikx/\hbar}$. A side note is that this potential-free Hamiltonian has a continuous spatial translational symmetry and therefore conserves momentum which additionally implies that eigenstates of this Hamiltonian are also eigenstates of the momentum operator $\hat{p}$ [§]

Once the lattice depth is non-zero, this symmetry is broken such that the Hamiltonian only retains a discrete translational symmetry. The Bloch theorem states that since the Hamiltonian (1.4) has a discrete translational symmetry from the periodic potential (1.3), then the eigenfunctions of the Hamiltonian will also be eigenfunctions of this discrete translation and hence will also be periodic

[‡]This is k-vector is defined as $2\pi/\lambda$ when the light used to create the potential originates from two counter-propagating lasers where $lambda$ is the laser wavelength. However, this only provides an upper-bound for what k-vector can be produced by a given laser wavelength. What matters is the k-vector in the plane of the lattice formed by the lasers which can be tuned by their relative angle. This point will be further elucidated in Ch. 3.

[§]This is, of course, obvious since the Hamiltonian is composed of only the momentum operator $\hat{p}$. However, the statement about translational symmetry in space and conserved momentum is a general one and quite powerful.

(1.5).

$$\phi_q^{(n)}(x) = e^{iqx/\hbar} \cdot u_q^{(n)}(x) \tag{1.5}$$

The Bloch wavefunctions, $\phi_q^{(n)}$ are labeled by their band index n and their quasi-momentum, or crystal momentum, q. This quasi-momentum is akin to the linear momentum of the free-particle case referenced to above except that it is now only defined within the Brillouin zone of the periodic potential $-\hbar k_L \leq q \leq \hbar k_L$ where k_L is the k-vector of the lattice. The function $u_q^{(n)}(x)$ is a Fourier series with a periodicity that correspond to multiples of the lattice period. Intuitively, this high-frequency cut off when $q = \pm k_L$.

To find the eigenfunctions of this new Hamiltonian with momentum states coupled by multiples of twice the lattice period, we can more conveniently solve this problem in Fourier space and solve for the eigenergies $E_q^{(n)}$. We first write both the potential and the periodic function $u_q^{(n)}(x)$ as Fourier series:

$$V(x) = \sum_m V_m e^{i2mkx} \tag{1.6}$$

and

$$u^{(n)}(x) = \sum_l c_l^{(n,q)} e^{i2lkx} \tag{1.7}$$

The periodic potential term $V(x)$ in (1.6) only has two non-zero terms that correspond to the lat-

tice periodicity ($V_{m=-1} = V_{m=1} = -V_o/4$). To find the coefficients for the Fourier series of $u_q^{(n)}$ and the eigenenergies $E_q^{(n)}$ one should exploit the orthogonality relation between Fourier modes after taking the inner-product of $\langle e^{i2l'kx}|H|\phi_q^{(n)}\rangle$ (please refer to Appendix C. This procedure results in:

$$\sum_{l}^{'} H_{l,l'} \cdot c_l^{(n,q)} = E_q^{(n)} c_l^{(n,q)} \tag{1.8}$$

where

$$H_{l,l'} = \begin{cases} (2l + q/k)^2, & l = l' \\ -V_o/4, & |l - l'| = 1x \end{cases} \tag{1.9}$$

Diagonalizing the Hamiltonian (1.9), where l and l' are matrix indices, will solve for the eigenenergies that depend on the continuous variable q and the discrete index n which labels the characteristic formation of *bands* in the spectrum. To gain some intuition for the system this Hamiltonian describes, we can first think about the $V_o = 0$ case. In the case of no external potential, this Hamiltonian will realize a parabolic dispersion curve in k-space from the momentum of a free-particle. By turning on the lattice potential $V_o \neq 0$ the external potential can now provide momentum kicks to the particle's wavefunction in discrete quant of $2\hbar k$ (when the indices l, l' differ by 1). In the case that the energy from the free-particle dispersion curve at q and $q \pm 2\hbar k$ are $\lesssim V_o$, then these two momentum states are strongly coupled and these states hybridize to make form an eigenstate. The first happens is at the $q = \hbar k$ point in the dispersion curve and defines what is know as the Brillouin

zone boundary in a crystal. Physically, this hybridization corresponds to perfect Bragg reflection of the particle's wave function at the Brillouin zone boundary. This hybridization forms the familiar *gaps* associated between bands of energy as defined on a reduced Brillouin zone band diagram (1.1).

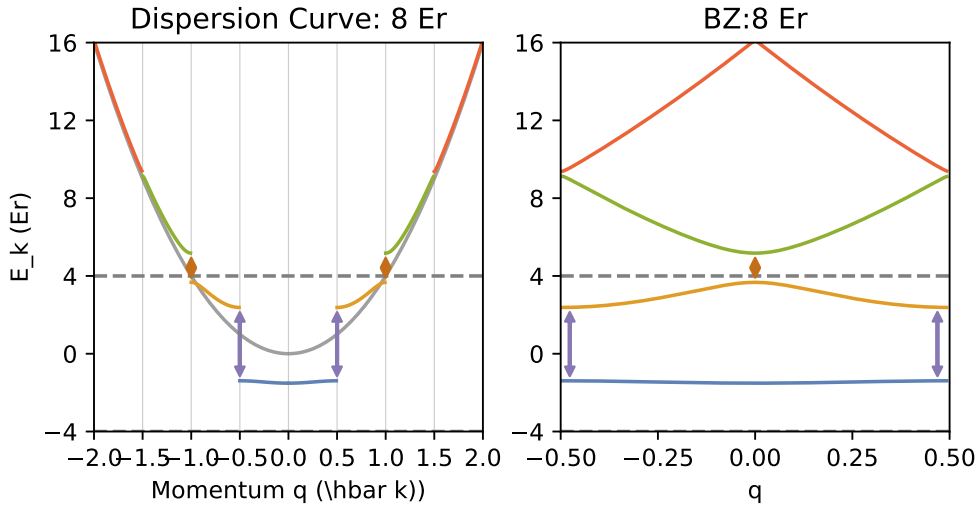

Figure 1.1: Dispersion with Bragg reflection. a, The left curve shows free-particle dispersion parabola + gaps opening up from Bragg scattering off the lattice. Additionally, the dashed-grey lines show the height of the lattice as it is centered about zero and determines when a state $|\psi_k^{(n)}\rangle$ is bound to the lattice. In this case ... This depiction of the hybridization of the free-particle dispersion curve is known as the extended Brillouin zone scheme and is an intuitive way of how to reach the notion of bands from Bragg scattering. **b** depicts the more familiar reduced Brillouin zone scheme associated with condensed matter physics and band structure. This mapping is both compact and conceptually reflects the notion of periodic states that are described by Bloch wavefunctions $|\phi_q^{(n)}\rangle$ that are only well defined for quasi-momentum states q that are bounded by the lattice wave-vector k_L.

Once the lattice depth, V_o, is deep enough that an entire band lies within its energy window, it conceptually makes sense to describe these as Bloch functions that are bound to the lattice and are the free-particle states dressed by free-particle states with integer multiples of the lattice vector $2\hbar k$. This is shown for both the ground band and the first excited band in in Fig. 1.1. This thesis will use the convention that $n = 0$ refers to the ground-band. These periodic eigenstates of

the Hamiltonian are plotted for various quasi-momentum states for both the ground band and the excited band in Fig. ??. A common physical picture given for the opening of a gap at the edge of the Brillouin zone is given by the phase of the Bloch wavefunction's spatial structure. While $|\phi_{q=\hbar k}^{n=0,1}(x)\rangle \approx e^{ikx} + (-1)^n e^{-ikx}$ are both composed of the same free-particle momenta states, their symmetric versus anti-symmetric superposition either concentrates the density of the particle either in the minima or the maxima of the lattice potential (as shown in Fig. 1.2).

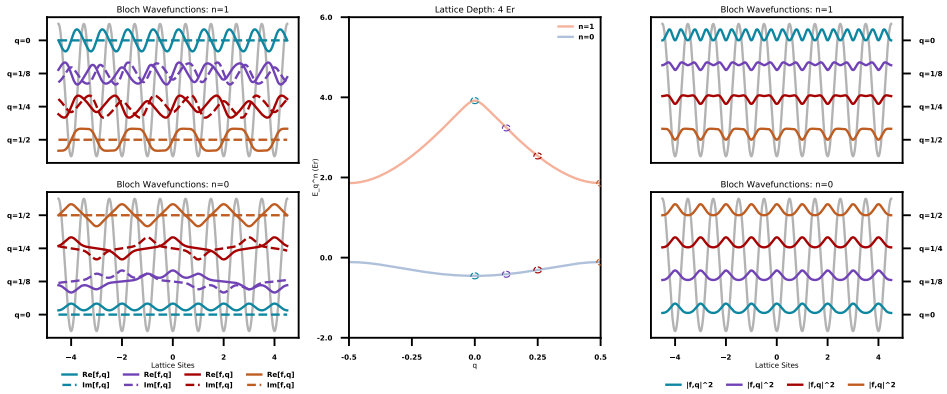

Figure 1.2: Bloch wavefunctions. a, The left plots depict the real and imaginary parts of the Bloch wavefunction's ($|\phi_q^{(n)}(x)\rangle$) spatial dependence as a function of distance for various quasi-momenta and both the $n = 0$ and $n = 1$ bands at a lattice depth of $4E_r$. **b** Plots the band structure for at $4E_r$ and the quasi-momenta the plotted Bloch wavefunctions describe. **c** These right plots depict the density distribution of the Bloch functions for the same quasi-momenta as the left plots and same bands. Note that the ground-band, $n = 0$, is well bound to the lattice and relatively "flat". This qualitatively means that the distribution of the ... for both a and c describe that the periodicity is basically the same, in the deep limit it is only the phase that appreciably changes.. Something something cosine dispersion.

There are two primary quantities that are typically extracted from the band structure due to their physical relevance: the band width and the band gap. The band width, the energy difference between the maximum and minimum energy for a given band ($arg\max_q \left\{E_q^{(n)}\right\} - arg\min_q \left\{E_q^{(n)}\right\}$), describes the maximum kinetic energy of a particle in that band. The kinetic energy becomes sub-

stantially suppressed as bands become bound to the lattice and will appear as approximately flat. The band gap, the energy difference between successive bands $\Delta = E_q^{(n+1)} - E_q'^{(n)}$ defines how well separated a particle in one band is energetically from another band. Practically speaking, all the physics in this thesis will assume a single-band model where all particles inhabit the ground-band of the lattice. This makes the band gap a relevant metric for determining how well the observed phenomena will be described by a single-band and how susceptible the system will be some form of heating that will deposit energy into the system. The evolution of the band gap and band width can be seen from progression of band structure plots in Fig. 1.3 as well as the evolution of the band gaps between various successive bands as a function of lattice depth.

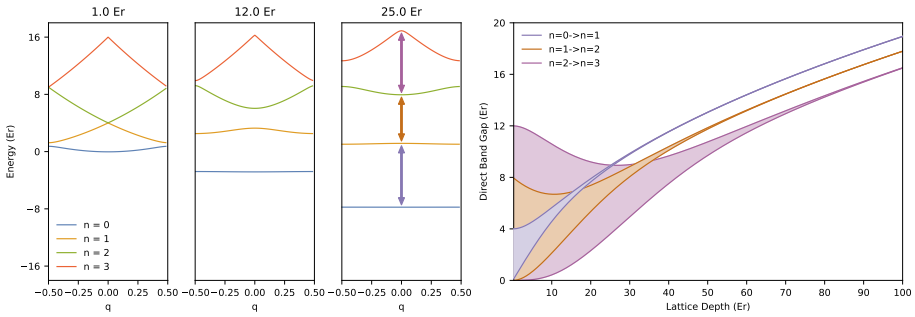

Figure 1.3: Band Gaps. a, The band structure of the four lowest bands are plotted for three lattice depths to depict how both the band widths and band gaps change as a function of lattice depth. Note that the lower bands both flatten and become gapped from the excited bands more quickly as a function of lattice depth. **b,** The band gap between successive bands can strongly depend on which quasi-momentum is being excited from and to ($\Delta_{q,q'}^{n,n+1} = E_q^{(n)} \rightarrow_{q'}^{(n+1)}$). In principle both direct, quasi-momentum preserving, and indirect, non quasi-momentum preserving, excitations are possible in a lattice. However, in the case of a simple sinusoidal lattice, both the minimum and maximum band gaps are captured by just analyzing direct band excitations. The minimum and maximum band gaps are plotted as the solid lines and the distribution of all intermediate possible values are plotted as the shading.

1.1.3 Wannier wavefunctions

The Bloch wavefunctions, as the single-particle eigenstates, are a convenient way to describe the physics of a particle in a periodic potential. They are a complete set of energy eigenstates and completely described by their band index n an quasi-momentum q. Since they are defined by a single quasi-momentum number q, they are maximally localized in momentum space and maximally delocalized in position space. An useful alternative, orthonormal basis for this system is given by the set of functions that describe the particle as localized in position space. These set of functions are known as Wannier functions and are a convenient way to describe the wavefunction of a particle in a band n that is maximally localized at a lattice site x_i. This basis can be constructed from a superposition of all Bloch wavefunctions within the Brillouin zone for a given band n:

$$w_n(x - x_i) = \frac{1}{\mathcal{N}} \sum_q e^{-iqx_i} \phi_q^{(n)}(x) \tag{1.10}$$

.

The normalization factor N depends on the finite number of quasi-momentum Bloch wavefunctions summed over. There are some additional subtleties that revolve around practically constructing these functions numerically and are elucidated in more detail in Appendix C. Additionally, since the Bloch wavefunctions are eigenstates of the original Hamiltonian, they may have been solved with an arbitrary global phase that will become an important relative phase in the construction of the Wannier functions $w_n(x - x_i)$. Thankfully, there is a convenient recipe to follow that es-

tablishes how to choose the phases when constructing $w_n(x - x_i)$ that produces a wavefunction maximally localized on site x_i.

We have seen from the symmetry of the periodic potential, the hybridization of the free-particle states at the edge of the Brillouin zone, and the plots of the Bloch functions in Fig. 1.2 that the wavefunctions of even bands ($n = 2 \times m, m \in \mathbb{Z}$) are also even functions of x and the wavefunctions of odd bands are also odd functions of x. The Wannier functions will also retain this symmetry since they are constructed from the Bloch functions within a given band. To then construct a maximally localized wavefunction at lattice site x_i, we must find the necessary phases multiplied by the Bloch wavefunctions that constructively add at $x = x_i$. For even bands, this we a phase for each Bloch function that makes it both real and positive at $x = x_i$. [¶] For odd bands, the Bloch wavefunctions are also odd about the center of each lattice site $x = x_i$. The recipe used above is modified such that the phase chosen is such that the first derivative of the Bloch wavefunctions are real and positive at site x_i. Including the recipes described above we can write down the Wannier functions construction as follows:

$$w_n(x - x_i) = \begin{cases} \frac{1}{N} \sum_q e^{\left(-iArg[\phi_q^{(n)}(x_i)]\right)} \cdot \phi_q^{(n)}(x), & n \text{ is even} \\ \frac{1}{N} \sum_q e^{\left(-iArg[\partial\phi_q^{(n)}(x)/\partial x|_{x=x_i}]\right)} \cdot \phi_q^{(n)}(x), & n \text{ is odd} \end{cases} \tag{1.11}$$

The Wannier wavefunctions represent the maximally localized, conjugate basis to the Bloch wavefunctions. These Wannier states become more localized for increasing lattice depth, which is plotted

[¶] It doesn't actually matter which phase you pick for this site, just that you rotate all Bloch wavefunctions such that their phase is the same at $x = x_i : Arg\left[\phi_q^{(n)}\right] = const. \forall\, q$ where $const. \in \mathbb{C}$

in Fig. 1.4a for the ground band. We can see additionally see plotted in Fig. 1.4 for a $45E_r$ lattice how the Wannier wavefunctions are also successively wider for higher bands in the lattice.

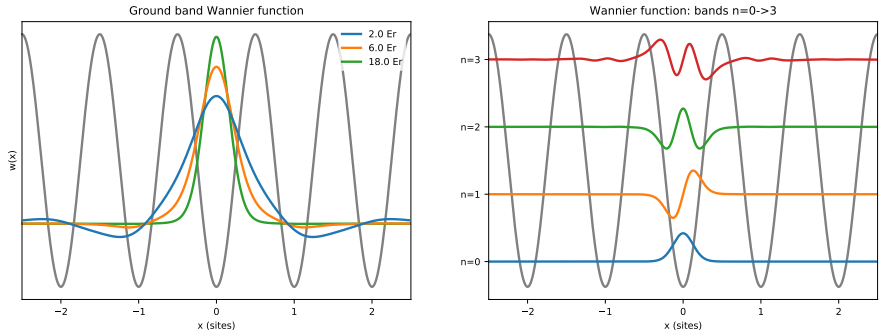

Figure 1.4: Wannier wavefunctions. a, .

A few useful observations can also be made from both the analytical form of $w_n(x - x_i)$ (1.11), the bands from which they are constructed (Fig. 1.1) that coincide with their plots in Fig. 1.4. Since successively higher bands are mapped from a higher, but limited range, of free particle momenta, we see that $w_n(x - x_i)$ must contain only Fourier components that correspond to the range $n \cdot \hbar k_L \leq k \leq (n+1) \cdot \hbar k_L$. Hence, the Wannier functions for successively higher bands, while still maximally localized, contain a corresponding wrapping of the wavefunction by n cot π. Additionally, as the lattice depth becomes much larger than the band width of a given band, the Wannier functions approach the wavefunctions of a Harmonic oscillator, as can be seen by the similarity between the similarity between the $w_n(x - x_i)$ plotted in Fig. 1.4b and Hermite Gaussians.[‖] Lastly, while the Wannier functions are not eigenstates of the original Hamiltonian, they become asymptotically

[‖]This is additionally a conceptually comforting fact as the cosine potential providing the lattice can be approximated to lowest order as a quadratic potential. However, due to the finite depth of the lattice, there is always a non-negligible amplitude in the wings of $w_n(x - x_i)$ that is necessary for an accurate description of the system

close as $V_o \rightarrow \infty$, where both the corresponding band becomes flatter and the associated Bloch wavefunctions will be nearly degenerate.

1.2 The Bose-Hubbard model

The treatment for deriving band structure and Bloch wavefunctions describe the entire physical story for a single-atom in an optical lattice. However, it neglects the many-body physics associated with interacting particles that leads to celebrated exotic condensed matter systems. It additionally does not easily lend itself to describing the nature of inter-particle interactions that are often derived from a local, inter-particle potential. To incorporate these local dependencies, we will now reformulate the free-particle Hamiltonian from before into a local basis that utilizes our derivation of the Wannier functions in the previous section.

In particular, we will describe the overlap of an atom's wavefunction with a local Wannier function defined about a particular lattice site as the population of the atom in an orbital about that site. This leads us towards adopting the tight-binding lattice model for bosonic particles that is known as the Bose-Hubbard model. This is a renowned toy condensed matter model that faithfully incorporates strong inter-atomic interactions that lead to strongly correlated states that are otherwise absent in interaction corrected mean-field equations, such as the Gross-Pitaevski equation (ref someone besides Philipp, Jacksch et al).

1.2.1 Interacting atoms in an optical lattice

In all our experiments, we work with dilute atomic gases. In these dilute gas regimes, the atom-atom interactions can be described be an effective inter-atomic potential between any two particles $V(\mathrm{r},$ where r is the inter-particle distance. This potential is strongly repulsive at distances on the order of a few Bohr radii, $(\sim\ a_o)$, due to the strong Coulomb interaction between the respective atom electron clouds. However, since atoms are polarizable, they are attractive at long distances due to the mutually induced dipoles that lead to a van der Walls force (ref rma 26).

In the case of low temperature regime utilized by ultracold atom experiments, these inter-atomic interactions primarily result in elastic scattering processes between the atoms. In this regime, it isn't necessary to know the exact shape of the interatomic potential since the low kinetic energies of the atoms do not enable them to probe past the centrifugal barrier. This means that only the lowest partial wave scattering process, *s*-wave scattering, significantly contributes to the inter-atomic interactions. Therefore, this contribution can be well approximated by a contact interaction that is characterized by a single parameter that quantifies the *s*-wave scattering length, a_s:

$$V(\mathrm{r}) = \frac{4\pi\hbar^2 a_s}{m}\delta(\mathrm{r}) \tag{1.12}$$

They are often tunable (ma citation 12) via Feshbach resonances where the interaction strength can be changed by many orders of magnitude and even change sign. Unitary limit. We determine our interaction strength via the lattice depth **.

**Explain ^{87}Rb problem for Feshbach resonances

1.2.2 Deriving the Bose-Hubbard model parameters

We can derive the Bose-Hubbard model by incorporating the inter-atomic contact interactions into the Hamiltonian of a bosonic field $\hat{\Psi}(x)$ and an external potential:

$$H = \int d^3x\, \hat{\Psi}^\dagger(x) \left(-\frac{\hbar^2}{2m}\nabla^2 + V(x) \right) \hat{\Psi}(x) + \frac{1}{2}\frac{4\pi\hbar^2 a_s}{m} \int d^3x \int d^3x'\, \hat{\Psi}^\dagger(x)\hat{\Psi}^\dagger(x')\delta(x-x')\hat{\Psi}(x)\hat{\Psi}(x') \tag{1.13}$$

Here the potential contains both the lattice potential and any additional potential term applied on top of the lattice that is relatively weak and spatially varies more slowly than the lattice itself: $V(x) = V_{latt}(x) + V_{arb}(x)$. In the low temperature regime, the atoms only populate the ground band and we can restrict this derivation to involving only basis states that overlap with this band. Since the interaction term is entirely local it is convenient to expand the bosonic field $\hat{\Psi}(x)$ in terms of ground band Wannier wavefunctions:

$$\hat{\Psi}(x) = \frac{1}{\mathcal{N}} \sum_i \hat{a}_i w_o(x - x_i) \tag{1.14}$$

Here $\hat{a}_i$ ($\hat{a}_i^\dagger$) are the annihilation (creation) operators for a boson in the ground band Wannier function cetreed at a lattice site x_i. These operators follow the typical bosonic commutation relation $[\hat{a}_i, \hat{a}_j^\dagger] = \delta_{i,j}$. This expansion allows us to rewrite 1.13 in terms of these bosonic annihilation and creation operators:

$$H = -\sum_{i,j} J_{i,j}\hat{a}_i^\dagger \hat{a}_j + \sum_{i,j,k,l} \frac{U_{i,j,k,l}}{2}\hat{a}_i^\dagger \hat{a}_j^\dagger \hat{a}_k \hat{a}_l + \sum_i (h_i - \mu)\hat{a}_i^\dagger \hat{a} \tag{1.15}$$

The additional potential that was added on top of the lattice, $V_{arb}(x)$, provides a variation in the on-site energy potential h_i. The chemical potential μ is a thermodynamic quantity that constraints the total particle number in the grand canonical ensemble description of the model. The $J_{i,j}$ term is known as the tunneling matrix element quantifies the tunneling rate between any two sites i and j and describes the kinetic energy of the atom. The $U_{i,j,k,l}$ term describes the various interaction matrix elements between atoms on sites i, j, k, l. Although the Wannier functions are all orthogonal, they were never eigenstates of the original Hamiltonian. Formally then, we can quantify these matrix elements via the overlap of the Wannier function after the Hamiltonian has acted on them:

$$J_{i,j} = -\int d^3x\, w_0^*(x - x_i)\left(-\frac{\hbar^2}{2m}\nabla^2 + V_{latt}(x)\right) w_0(x - x_j) \tag{1.16}$$

$$U_{i,j,k,l} = \frac{4\pi\hbar^2 a_s}{m}\int d^3x\, w_0^*(x - x_i) w_0^*(x - x_j) w_0(x - x_k) w_0(x - x_l) \tag{1.17}$$

For nearly all practical cases, we will work in the "tight-binding" regime of this ground band model. This approximation assumes that the Wannier functions are sufficiently localized that all higher order tunneling processes and higher order interaction terms may be ignored. This leave the model with only a nearest-neighbor tunneling $J_{i,i\pm1} \equiv J$ and on-site interaction $U_{0,0,0,0}] \equiv U$ and results in the stand form of the celebrated Bose-Hubbard model:

$$H_{BH} = -J \sum_{\langle i,j \rangle} \hat{a}_i^\dagger \hat{a}_j + \frac{U}{2} \sum_i \hat{n}_i(\hat{n}_i - 1) + \sum_i (h_i - \mu)\hat{n}_i \tag{1.18}$$

where $\hat{n}_i = \hat{a}_i^\dagger \hat{a}$ is the on-site number operator and the bracket sum, $\langle i, j \rangle$ refers to a sum only over neighboring indices. Physically, the mechanism that describes the exact contributions for the on-site interaction term comes from the sum of all pair-wise interactions of n atoms on site i, each of which contribute an energy cost of U : $U \sum_i \binom{\hat{n}_i}{2} = U \sum_i \frac{\hat{n}_i!}{(\hat{n}_i - 2)!2!}$.

Both parameters J and U change significantly as a function of the lattice depth V_o. The qualitative features of the states that are harbored by the Bose-Hubbard model depend only on the ratio of these two quantities U/J. Practically speaking, the absolute energy scales of these two parameters are important for defining relevant experimental time-scales. This conversion comes from defining all energies by $\hbar$ as an *angular* frequency. In our experiment, the depth of the lattice is measured in lattice recoil $E_r/\hbar \approx 2\pi \times 1240$Hz and sets these overall energy scales. The values for J and U, as calculated from the ground state Wannier wavefunctions (1.16, 1.17), are plotted for the parameters of our experimental parameters in Fig. 1.5.

In the deep lattice (tight-binding) limit, the dispersion of the ground band becomes well approximated by a cosine potential, $E_q = -2J \cos(2\pi q/k_L)$ where J is the Bose-Hubbard hopping parameter. In this regime can be solved for exactly and approximately decays exponentially with lattice depth:

$$J = \frac{4}{\sqrt{\pi}} E_r \left(\frac{V_o}{E_r} \right)^{3/4} e^{-2(V_o/E_r)^{1/2}} \tag{1.19}$$

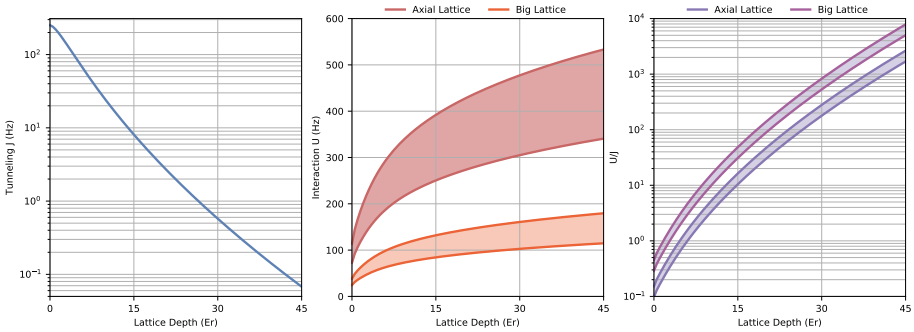

Figure 1.5: Bose-Hubbard Parameters. a, All plotted for a 1-D Lattice.

Additionally, the scaling of U with lattice depth can be estimated by approximating Wannier wavefunctions with the Harmonic Oscillator Gaussian states. In this limit the two relevant comparisons to the lattice can be given by the effective on-site trap frequency ω_{ho} and oscillator length l_{ho} that depend on the lattice depth:

$$\omega_{ho} = 2E_r\sqrt{V_o/E_r} \tag{1.20}$$

$$l_{ho} = \sqrt{\hbar/m\omega_{ho}} = \frac{a/2}{2\pi}\left(\frac{V_o}{E_r}\right)^{-1/4} \tag{1.21}$$

$$w_n(x - x_i) \approx \psi^n_{l_{ho}} = \frac{1}{\sqrt{2^n n!}}\left(\frac{1}{\pi l_{ho}^2}\right)^{1/4} e^{-x^2/(2l_{ho}^2)} H_n(x/l_{ho}) \tag{1.22}$$

where $H_n(x/l_{ho})$ are the Hermite polynomials of order n.

This leads to an approximate scaling of $U \propto V_o^{1/4}$. This elucidates the point that while both J

and U are tunable with lattice depth, the relevant ratio of U/J is mostly determined by the exponential suppression of J with the lattice depth. However, one difference is that J depends only on the lattice depth along the direction it defines tunneling. This is not the case for U which is nonlinear and depends on the integral of the Wannier wavefunction in all three dimensions. This means that even without using a Feshbach resonance, there is some marginal tunability of U by just changing the lattice depth in the dimensions orthogonal to the dimension of interest. This is particularly relevant since the majority of the work described in this thesis is performed for one dimension. The lattices that provides confinement along the z-direction has the widest range of tunability and is plotted in Fig. 1.5 as two-bands of experimentally accessible ranges.

1.3 Quantum phase transitions: superfluid to Mott-insulator

Quantum phase are a celebrated achievement in physics that differ from their classical counterparts since they can occur even at zero temperature. These quantum phase transitions are driven by quantum fluctuations in the ground state wavefunction of a system since all thermal fluctuations are frozen out at zero temperature. The Bose Hubbard model famously exhibit two distinct quantum phases that depend on the relative strengths of the on-site interaction and tunneling terms. This will first be described by the ground state wavefunctions behavior in the two extremes for a lattice with no additional potentials, $h_i = 0$, N atoms, and periodic boundary conditions.

1.3.1 Superfluid phase: $J \gg U$

In the limit of very large J compared to U, the Hamiltonian favors the delocalization across the lattice. The ground state wavefunction becomes simple to write down in the extreme case that $U \rightarrow 0$ and we recover atoms occupying the Bloch band for $q = 0$ as defined from the band structure derived earlier in this chapter:

$$|\Psi_{SF}\rangle = \frac{1}{N}\left(\hat{a}^{\dagger}_{q=0}\right)^{N}|0\rangle \propto \frac{1}{N}\left(\sum_i \hat{a}^{\dagger}_i\right)^{N}|0\rangle \tag{1.23}$$

where $|0\rangle$ is defined as the vacuum state with o bosons. In the case that we don't restrict the ground state to a specific number of particles N, the ground state is defined by a coherent state $|\alpha_i\rangle$ on every site i since this state is an eigenstate of the tunneling matrix elements $\hat{a}_i$. In this regime of uncertain particle number the ground state becomes a product state of coherent states:

$$|\Psi_{SF}\rangle \approx \prod_i |\alpha_i\rangle = \prod_i e^{-|\alpha_i|^2/2} e^{\alpha \hat{a}^{\dagger}_i}|0\rangle \tag{1.24}$$

where the phase of α is well defined and constant across all sites in the lattice ($\hat{\phi}|\alpha_i\rangle = Arg[\alpha_i]$) and a fixed average density $\langle n\rangle = |\alpha|^2$. This approximation conceptually describes the superfluid as an array of Bose-Einstein condensates on each lattice site with a well defined phase locked across the entire lattice via the tunneling term. The superfluid phase is defined by a non-zero order parameter $\psi \equiv \langle\alpha\rangle$ and has characteristic properties of having gapless excitations and finite compressibility $\kappa = \partial n/\partial\mu$.

1.3.2 Mott-insulator: $U \gg J$

In the opposite limit, as U becomes the dominant energy scale in the system, the eigenstates of the ground state become defined by the on-site atom number. This forms an insulating state that suppresses particle transport due to the strong inter-atom interactions. This becomes clear in the extreme limit as $J \to 0$ and the Hamiltonian is now defined by only the on-site number operator $\hat{n}_i$ meaning that all the eigenstates of the Hamiltonian are also eigenstates of $\hat{n}_i$. Since the on-site particle number is quantized, the atom-number on a given site i is determined by the ratio of μ/U. In the case of a commensurate total atom number N with the number of lattice sites ($N/L = n$), the Mott-insulator wavefunction is written as:

$$|\Psi_{MI}\rangle = \prod_i \left(\hat{a}_i^\dagger\right)^n |0\rangle \tag{1.25}$$

In the Mott-insulating state, the order parameter in the ψ from the superfluid goes to zero since all phase coherence between lattice sites is lost. In the case of commensurate filling, this state forms of plateaus of fixed on-site atom number n and the lowest excitations are defined by moving a particle to a neighboring site at the cost of the on-site interaction energy U. This defines this state as having gapped excitations and points to its *in*compressibility.

1.3.3 Phase Diagram

The two variables, phase ($\hat{\phi}$) and on-site atom number ($\hat{n_i}$), are conjugate variables that describe the quantum phases described above. The diagram that determines the boundary between the phases

can be understood from a mean-field approach. The superfluid to Mott insulator transition is a second order phase transition and therefore can be described by a Landau approach (cite Landau?)

The mean-field phase diagram is plotted in Fig. 1.6 with axes given by the relative chemical potential μ/U and relative tunneling strength zJ/U where z is the coordination number, the number of neighbors to each lattice site, which is equal to the physical dimensionality in a square lattice ($z = D$). The derivation of this diagram shown in more detail in appendix (bla bla). The lobes on the left plot of Fig. 1.6 define plateaus of a given atom number which become smaller, or experimentally more fragile, as a function of on-site occupation number (seen as the cross section in chemical potential μ/U in the figure).

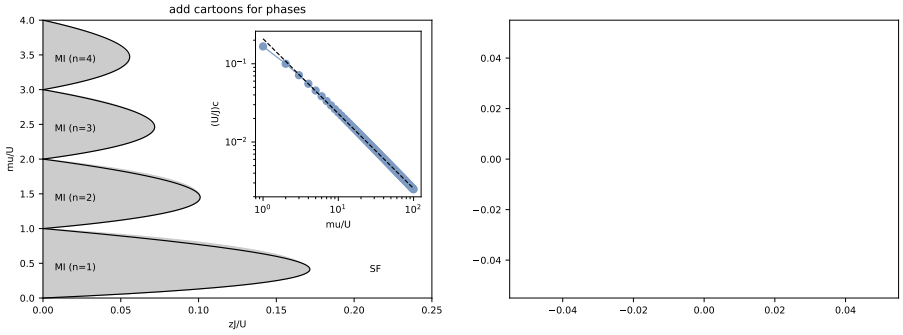

Figure 1.6: Mean-Field Phase Diagram. a,

It can be seen intuitively that the critical, finite value of U/J_c depends on the on-site occupation number by comparing the kinetic energy scales to the gap in the system. We first start in a Mott-insulating plateau $|\Psi_{MI}\rangle$ with n atoms per site which has a total energy of $E_0 = L \cdot Un(n-1)$. The first excitation from this state involves moving an atom from site i to its neighbor and has a total energy of $E_1 = (L-2) \cdot Un(n-1) + U(n+1)(n) + U(n-1)(n-2)$. The gap

between these two states is given by $\Delta = E_1 - E_0 = U$ and notably is independent of the on-site occupation number n! Since the atoms are bosonic and identical, the kinetic energy term J that connects these two states has a bosonic enhancement factor of $\sim n$ and means that the relevant comparison for distinguishing these two phases is $(U/J)_c \propto U/(nJ)$. The peaks of the lobes in Fig. 1.6 and are plotted as a function of half integer chemical potential in the inset and agree with a power law exponent n^{-1}.

1.4 Beyond flat, tight-binding Bose-Hubbard

Bose-Glass?

off-site interaction, more than nearest neighbor tunneling, dipole moments?

Disorder effects on J and U cite De Marco, high-order tunneling, tilt and tunneling to higher bands

heating rates, probably refer to appendix

2

Quantum gas microscope:

an overview

All experiments presented in this thesis are performed using an apparatus designed in a quantum gas microscope architecture for bosonic atoms.* We study at a degenerate, quantum gas of ^{87}Rb atoms in either one or two dimensions by confining the atoms to a single-plane in a three-dimensional optical lattice. This single-plane of ultracold atoms lies at the focus of an imaging system with a high numerical aperture (NA) of 0.8. The occupation of these lattice sites can be readout with single-site resolved resolution via an in-situ fluorescence imaging technique. A far more detailed description of this apparatus are provided in a number of other publications (ref people) and only the core components necessary to explain the successive work of this thesis will be explained here.

While all ultracold atom machines are an amalgamation of many parts that collectively record the successes of atomic physics for the past several decades, the schematic in Fig. 2.1 only represents the latest addition and the heart of the experimental apparatus. This schematic shows the high-NA imaging objective that sits outside an evacuated glass cell in which the degenerate quantum gas is formed. The custom objective that sits outside the glass cell has an NA ≈ 0.55. The in-vacuum hemispherical lens is made of fused silica with a refractive index of $n = 1.45$ and increases the combined NA to ≈ 0.8. We create a Bose-Einstein condensate (BEC) of ^{87}Rb by conventional evaporation in a magnetic trap that resides at the focus of this imaging system which is $\approx 10\mu m$ below the bottom surface of the hemisphere. The z-confining lattices enter into the glass cell from

*Traditional microscope naming conventions typically refer to the method by which they probe the phenomena of interest (i.e. *optical* microscopy, *electron* microscopy). Although this microscope may seem dissimilar to this naming convention, an important point of this apparatus is that it is using the quantum properties of the degenerate atomic gas to probe physics that is harbored by Hamiltonians of interest. While I don't think this name was intentionally chosen to reflect this approach, I think it is an accurate description.

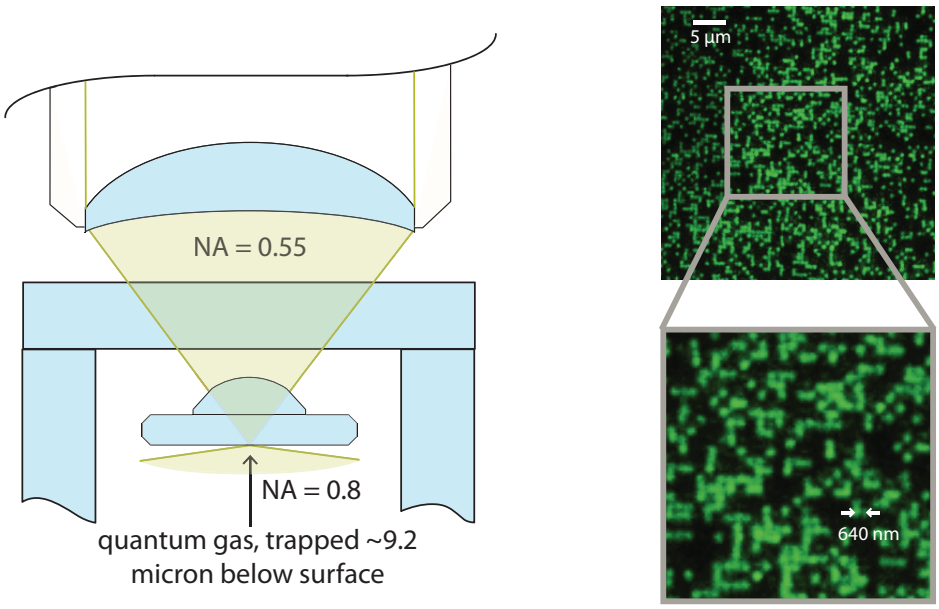

Figure 2.1: Schematic of Objective and Glass Cell. a, Heart of the quantum gas microscope

the sides while the $x - y$ plane lattices are projected through the objective itself. The occupation of the lattice sites are imaged onto an EMCCD camera (ixon whatever) using fluorescence imaging from polarization gradient cooling via optical molasses beams. These two paths are the two generic options for optical access to the atoms and all other beams are combined onto these paths by either beam-splitters or dichroic filters.

2.1 Optical lattice potentials

The dominant potential landscape experienced by the atoms is defined by optical lattices in three dimensions. The atoms are loaded from the BEC in a magnetic trap into a single two-dimension plane

by being confined by a single node of a vertical (z-direction) lattice. All studied physics relating to the Bose-Hubbard model derived in the previous chapter is restricted to within this two-dimension plane (x, y-direction). All lattices are formed by interfering two beams a long a given axis which produces a square lattice in all directions with a sinusoidal shape.

MAKE STATEMENT ABOUT PHOTODIODES SOMEWEHRE?

2.1.1 z-Lattices

The loading of the BEC into a single node of the z-confining lattices is conducted via a two-step process and requires two different z lattices. Both of these lattices are generated from a single beam that is reflected off the uncoated, flat surface of the hemispherical, in-vacuum lens as shown in Fig. 2.1.

The first step comes from a beam illuminating this surface from a very shallow angle and forms a large spacing lattice with a lattice constant of $\approx 9.2\mu$m which corresponds to a recoil energy $E_r \approx 2\pi \times 7$ Hz. This large spacing lattice is denoted as the "big" lattice. The atoms are loaded into the 1^{st} minimum of the lattice from this surface, which provides the reference for defining all z-positions in the apparatus. While this bottom surface is uncoated, the angle is sufficiently shallow ($\approx 88^\circ$ from normal) such that the Fresnel intensity reflection coefficient is reasonably large ($R_s \approx 0.85$). This reflection coefficient produces a lattice with a contrast of ≈ 0.997. This means that for a measured lattice depth of V_o^{big}, the corresponding DC offset will be $\approx 0.002 \times V_o^{big}$.

The second step involves a hand-off with a second beam that illuminates the surface from the opposite direction at a less shallow angle ($\approx 75.6^\circ$) to produce a lattice with a smaller lattice constant of $\approx 1.5\mu$m which corresponds to a recoil energy $E_r \approx 2\pi \times 255$Hz. This smaller spacing

lattice is denoted as the "axial" lattice. The atoms lie in the 6^{th} minimum of this lattice which overlaps with 1^{st} minimum of the "big" lattice. The uncoated surface has a more detrimental effect at this illumination angle where the Fresnel intensity reflection coefficient is much significantly smaller ($R_s \approx 0.39$). However, since the beam interferes with itself upon reflection, the interference contrast still remains relatively high at ≈ 0.90. This means for a measured lattice depth of V_o^{axial}, the corresponding DC offset will be $\approx 0.056 \times V_o^{axial}$. The angle dependencies of both of these parameters, minimum offset and contrast, are plotted in Fig. 2.2.

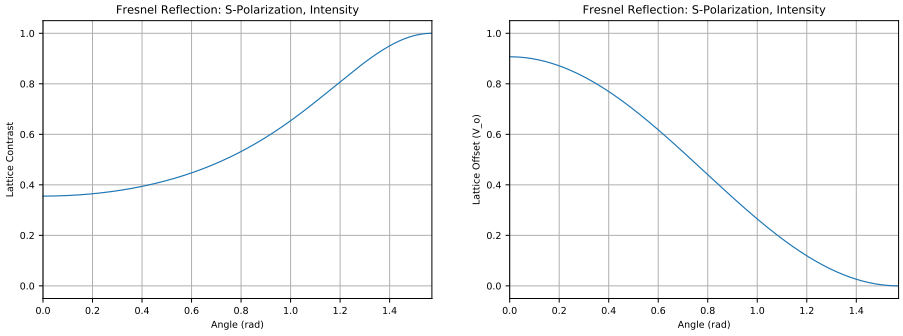

Figure 2.2: Lattice Parameters vs. Angle Rate a, Lattice Contrast **b,** offset in units of lattice depth

Both of these z-confining lattices are generated from an amplified Superluminescent Light Emitting Diode (SLED) source centered at $\lambda \approx 755nm$. The bandwidth of this light is relatively wide $\approx$ 3nm such that the light is approximately temporally *in*coherent. The corresponding coherence length is $\approx 100\mu$mwhich is much longer than the z-lattice spacing and allows for relatively high-contrast interference quoted above. This short coherence length, while allowing the creation of a high contrast lattice at the length scales of interest, it prevents interference of any of the conservative potential beams with one another or with reflections from surfaces more than 100μm away.

2.1.2 x, y-Lattices

In the $x - y$ plane, the lattices are imaged onto the atoms from a holographic mask through the objective (Fig. 2.1). The spacing of this lattice is $\approx$ 680 nm which corresponds to a recoil energy $E_r \approx 2\pi \times 1240 Hz$. The holographic mask is a phase hologram that imprints a square wave of alternating 0 and π phase onto the profile of the illuminating beam. This phase imprint nearly eliminates the 0^{th} order light emanating from the hologram and only the ± 1 orders are imaged on to the atoms. This produces a sinusoidal lattice with relatively high contrast due to the satisfaction of the imaging condition in the microscope. However, it additionally means that any unwanted artifacts (e.g. dust on the hologram) is additionally imaged onto the atom potential and creates local disorder. To alleviate some of this disorder, the beams are spatially filtered in the Fourier plane of the imaging system (cite 72 from philipp).

The same SLED source used to produce the z-confining lattices is also used to produce these lattices in the $x - y$ plane. Since the lattices are imaged onto the atoms, a more temporally incoherent source could, in principle, be used.

2.1.3 Disorder (unintentional) and heating rates

The use of temporally incoherent light alleviates the contribution of stray reflections to unwanted interference, and hence unwanted disorder, in the system. However, since the lattices themselves are imaged from a holographic mask onto the atoms, the fidelity of the lattice potentials is very sensitive to local scatters in the image plane of the imaging system. There are two approaches to alleviate this

problem: spatial filtering of the lattice beams in the Fourier plane of the system (currently implemented), or the illumination of the mask with spatially incoherent light that would average out any local scatterer.

Within the context of a faithful realization of the Bose-Hubbard model, the dominant effect from this disorder corresponds to a modulation in the on-site potential height h_i in the tight-binding limit. However, the choice of blue- or red-detuned lattices affect the relationship of h_i to the actual intensity of the scattered beam. In the case of red-detuned lattices, the atoms reside at the intensity maxima which means that, in the tight-binding limit, the on-site potential contains both the lattice depth $-V_o$ and the zero-point energy $\propto V^{1/2} \propto \hbar\omega_{ho}/2$. In a blue-detuned lattice, the atoms reside at the intensity minima and hence are sensitive to only the zero-point energy shift $\propto V^{1/2}$. This dependence is plotted in Fig. ?? as a function of scattered intensity ϵ difference between two beams interfering to produce the optical lattice. The light used to produce the lattices potentials in the experiment has a center frequency of $\lambda = 755$ nm which is far blue-detuned from atomic resonances of $\lambda_{D1} = 795$ nm and $\lambda_{D2} = 780$ nm.

The other relevant consideration for the faithful realization of the Bose-Hubbard model in optical lattices depends on residual spontaneous scattering of light from the lattices by the atoms. This light will necessarily impart some kinetic energy onto the atom and begin to populate higher bands in the lattice. This may appear, at first glance, to not be a significant issue in the case of a blue-detuned lattice since the atoms sit at the intensity minima. While the scattering rate is indeed significantly different for the blue- and red-detuned cases, the "heating" rate (rate at which atomic population is moved to higher bands) is not necessarily different (cite daley paper). This result of

equivalent "heating" for both blue- and red-detuned lattices corresponds only to the increase in average energy for an atom. However, it doesn't take into account the increase in entropy related to the dephasing of a many-body state evolving under the Bose-Hubbard model. This will become the metric of interest and therefore the scattering rate the more appropriate quantity for comparing between lattice detunings (Fig. 2.3).

We compare several methods for calculating the spontaneous scattering rate in the lattice. The first estimate that will be considered follows an assumption of deep lattices and being deep within the Lamb Dicke regime (cite Daley). Once you include the Lamb Dicke parameter, $\eta^2 = (4V_o/E_r)^{-1/2}$, the estimated heating rate for deep lattices is just:

$$\gamma = E_r \frac{\Gamma}{2\Delta} \left(\frac{V_o}{E_r} \right)^{1/2} \tag{2.1}$$

where Γ is the linewidth of the D2 transition (nearest resonance for the blue lattice), Δ is the detuning of the lattice light from the D2 transition, and E_r is the lattice recoil energy. In the case of the $x - y$ lattices, which should have no appreciable offset, this will become a good estimate of the spontaneous scattering rate as shown in Fig. 2.3. However, it is a poor description of the spontaneous scattering rate with an offset and so we take a more general approach that allows additional potential offsets (2.2).

$$\gamma = E_r \frac{\Gamma}{\Delta} \int dx \ \left(V_{latt}(x) + V_{offset} \right) |\psi(x)|^2 \tag{2.2}$$

where the considered $\psi(x)$ is either the Wannier wavefunctions, $w_n(x)$, or the Harmonic Oscil-

lator wavefunctions. These more accurate estimates from (2.2) are plotted in Fig. 2.3. The relevant lattice depths are: $\approx 2 - 45E_r^{x,y}$ for the $x - y$ lattices, $\approx 40 - 250E_r^{axial}$ for the axial lattice, and $\approx 3,000 - 20,000E_r^{big}$ for the big lattice.

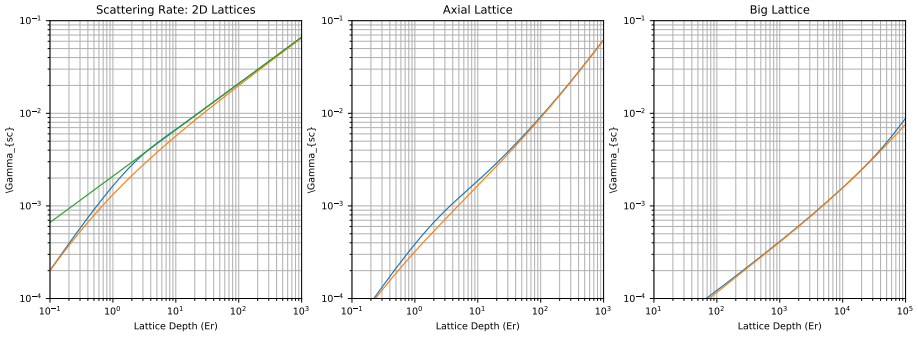

Figure 2.3: Spontaneous Scattering Rate a, 2D **b,** Axial, **c,** Big

Could make this statement that for the same scattering rate at the same lattice depth, you need to detune a red lattice such that $\Delta_R = \Delta_B(1+\eta^2)/\eta^2 = \Delta_B\left(1+\left(\frac{E_r}{4V_o}\right)^{1/2}\right)\left(\frac{E_r}{4V_o}\right)^{1/2}$

Lifetime from background collisions is $\approx 33(3)$s.

2.2 Arbitrary potential generation

The ability to realize interacting, many-body systems at ultracold temperatures has been the work horse of atomic gasses and allows the observation exotic physics such as the superfluid to Mott-insulator transition (cite markus and people). The addition of a microscope to these systems enables single-site resolution and access to the lattice sites in the system. Not only can this be used for imaging to determine which lattice sites are occupied by atoms, but by symmetry enables the microscope to be used in reverse to project local optical potentials on the order of a lattice site.

Using this capability for single-site optical potential projection has enabled a series of pioneering experiments that enable Hamiltonian engineering on top of the bare Bose-Hubbard model. This is implemented in our apparatus via a Digital Micromirror Device (DMD) that is located in the Fourier plane of our imaging system. Even though the DMD only provides a binary mask for projecting patterns onto the atoms, the fact that it is in the Fourier plane enables finer resolution for single-site features that are spread out across a significant portion of the DMD. Only a brief description of this setup will be mentioned here such that it provides context for how it is used in the successive experiments detailed in this thesis. A more detailed description of this setup can be found in the theses are article (ref other theses for technical details + philip zupancic paper).

The DMD is illuminated with a laser that is blue-detuned from the D1 and D2 transitions with a center wavelength $\lambda_{DMD} = 765$ nm. By placing the DMD in the Fourier plane of the imaging system, all desired potentials must be programmed as the Fourier transform of the desired potential at the atom plane. Additionally, the potential generation on the DMD incorporates an additional grating in the projection that allows for both amplitude and phase control of the light. Since it is really the *field* of the light that is tunable with the DMD, the patterns produced can be pre-compensated for aberrations in the imaging system such that the desired potentials is produced to a high fidelity. Aberrations in this system can be reduced to $\approx \lambda/10$ at the atom plane.

2.2.1 Disorder (intentional)

The DMD is used for two primary functions for the experiments in this thesis: 1) wall-like potentials that act to isolate sections of the optical lattices and 2) the generation of local, tunable "disorder" for

the realization of localized states in the Bose-Hubbard model. For all experiments in this thesis the applied potential used to localize the wavefunctions is sampled from a quasi-periodic distribution of on-site potentials.

2.3 Imaging and readout

At the end of every experimental sequence, the atoms are imaged via fluorescence imaging by optical molasses beams. The recoil of this near-resonant light necessarily and significantly excites the atoms to higher-bands in the optical lattice. Even though the optical molasses light provides polarization gradient cooling, the average energy would not remain trapped in the far from resonant lattices used for studying Bose-Hubbard model physics. To keep the atoms trapped to a single lattice site during imaging we use near-resonant lattices that are blue-detuned by ≈ 55 GHz from the $\lambda_{D1} = 795$ nm transition. The depth of this "imaging" or "pinning" lattice is $\approx 5000 E_r$. This light is generated by a verdi bla bla bla.

During the flourescence imaging process, an additional complication occurs for multiply occupied sites. The absorption of a photon by the atom leads to the formation of an electron dipole moment from the excited state. This, in turn, induces a dipole into a nearby atom on the same lattice site such that they form a molecular potential and causes the atoms to gain kinetic energy via their mutual attraction. However, the excited state will then decay on the order of linewidth. This process will quickly leave both atoms with enough energy to escape even the deep imaging lattice and is known as photo-assisted collisions (cite people). Importantly, this results in pair-wise loss from a

lattice site during imaging such that only the parity of the on-site occupation number is image and is known as "parity projection."

This parity projection imaging can be circumvented for one-dimensional slices of the lattice by using the DMD. The DMD is used to create two wall-like potentials that isolated a single row or column of the lattice. The corresponding lattice is then reduced in depth such that all other atoms outside of this isolated tube escape the system. Then the atoms within isolated tube are expanded along the orthogonal direction for a brief time such that they are very spread out over the orthogonal direction during the imaging sequence. This makes it very unlikely, in a probabilistic sense, for the atoms to occupy the same site and be ejected from the lattice due to the photo-assisted collisions. This expansion allows for on-site occupation number resolution. For a one-dimensional, many-body wavefunctions this amounts to a projective measurement on the particle number basis or Fock basis.

This resolution of the on-site number distribution enables several important key features for probing quantum many-body systems. It enables readout of the entire diagonal of full system's density matrix which allows for probing correlations within this basis. It also enables higher-fidelity state readout in two ways: during the imaging process there is a finite probability an atom hops to a neighboring site which can result in photo-assisted collisions and it also enables post-selection on total atom number. The former of these two considerations is shown by comparing the in-situ (parity projected) image versus the full counting image of a Mott-insulator (Fig. ??). The latter is an essential tool for reducing the heating that contributes to measurements in the experiments described later on in this thesis.

2.4 Calibration of energy scales

The ability to accurately determine all experimental parameters in the system is an invaluable benefit to the precision of the results generated by this experiment. I have briefly described many of the import calibration steps that were used ubiquitously throughout this thesis to accurately determine Bose-Hubbard parameters for conducting experiments and will not be described otherwise. Additionally, many of these methods are built upon previous results using the apparatus and in some cases are throughly detailed in those publications, which will be cited in the appropriate locations.

2.4.1 Lattice depth: Kapitza-Dirac Scattering

A particularly efficient method to calibrate the lattice depth experienced by the atoms is via Kapitza-Dirac scattering (cite gretchen campbell etc). This method requires that the atoms have Bose-condensed so that their many-body wavefunction has a well defined phase across the entire cloud. The lattice is then turned on very diabatically[†] and illuminates the atoms for a variable, but brief time period. This brief illumination of the atoms is such that the atoms only experience a potential that evolve the local phase of their wavefunction but the atoms have not had time to move yet. The imprinted phase on the atoms has a spatial structure that is proportional to the lattice potential and can be probed easily via common time of flight measurements which map the spatial Fourier components, or wavevectors of the wavefunction, to momentum.

This mapping of the imprinted spatial phase on the BEC to momentum has a convenient and

[†]This means the new Hamiltonian is turned on significantly faster than all the inverse energy scales in the system such the wavefunction itself has not evolved during the turn on time.

clean analytical form that results from the spatial phase always being commensurate with periodicity of the lattice. This results in the atomic momentum only being non-zero at integer multiples of the lattice wavevector. The population in these integer multiples then follows the analytic form given by:

$$P_{|\nu|}(t) = \left| \mathcal{J}_\nu \left(\pi E_r \frac{V_o}{E_r} t \right) \right|^2 \tag{2.3}$$

where $\mathcal{J}_\nu$ is the Bessel function of thest kind, ν denotes the integer of the lattice vector and the order of the Bessel function, V_o is the lattice depth in Hz, E_r denotes the recoil energy of the lattice, and t is the time the atoms have evolved in the presence of the lattice. The derivation of this form is shown in Appendix D. The evolution of the population into these modes is shown as a function of time in Fig. 2.4. As can be seen in this figure, the dynamics stop following the predicted evolution due to the presence of the additional trap confinement and that the wavefunction will also begin to redistribute atomic population in the presence of this lattice on the order of the local, lattice site trap frequency ω_{Latt}.

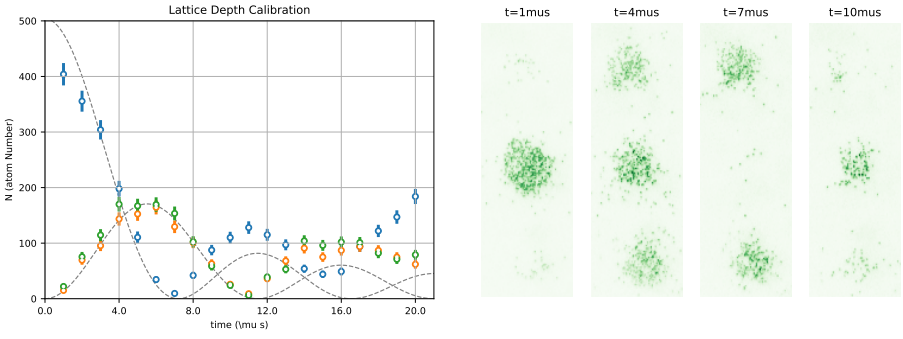

Figure 2.4: Kapitza-Dirac Scattering a,

2.4.2 Tunneling J : single-atom quantum walks

The tunneling matrix element(tunneling strength), J, can be calibrated from the quantum walk of single atoms in 1-D lattices. This protocol involves first isolating a single-atom at a particular site per 1-D lattice. These dynamics have been explore extensively in a number papers (cite Philipp, Yoav, and photon people) and of significant interest in their own right. While the tunneling strength and the lattice depth have a well defined theoretical relationship that could make this calibration seem redundant, practically speaking this method provides a far more accurate estimate of the local tunneling strength.[‡] The analytic form is quite similar to the Kapitza-Dirac scattering form (this is not by accident, please refer to the derivations in Appendix D):

$$P_{|\nu|}(t) = \left|\mathcal{J}_\nu\left(2 \times 2\pi J t\right)\right|^2 \tag{2.4}$$

where $\mathcal{J}_\nu$ is the Bessel function of thest kind, ν denotes the integer of the lattice vector and the order of the Bessel function, and J is the tunneling strength. There is an additional formulation that includes the possibility for local potential gradients that can provide a better fit and is the corresponding from for what are known as Bloch oscillations:

$$P_{|\nu|}(t) = \left|\mathcal{J}_\nu\left(\frac{2J}{\pi E}\sin\left(\pi E t/h\right)\right)\right|^2 \tag{2.5}$$

[‡]This is partially due to some of the systematic biases in the lattice depth calibration that uses Kapitza-Dirac scattering that limit the precision of the measurement. However, the other issue is that the optical lattices used in this apparatus have local variation in disorder that can locally modify the tunneling strength J. Since the vast majority of experiments in this system work with appreciably large-lattice depths and small systems, this is a significant consideration for calibrating experimental parameters.

where E is the local potential gradient. For a given evolution time t, a corresponding lattice size can be fit where $|\nu| \leq L/(2\pi J)$. [§] Theses fits and averaged site-occupation date are shown in Fig. 2.5. Note that at very low-lattice depths, the tight-binding, nearest-neighbor coupled Bose-Hubbard model becomes a less accurate description of the physics in the lattice and hence higher-order tunneling terms become significant. The deviation, both theoretical an measured, is shown in the figure.

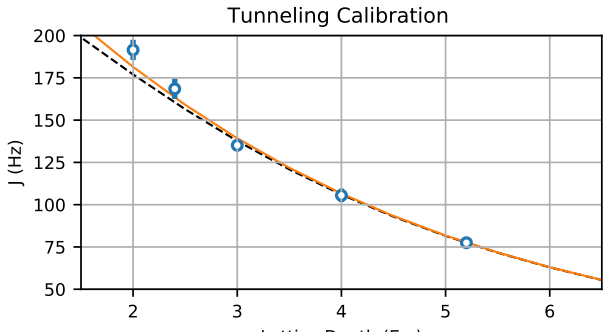

Figure 2.5: Quantum Walk a,

2.4.3 Interaction U and linear tilt E: photon-assisted tunneling

Determining the interaction strength U and local potential variation from disorder can be determined from a single protocol that utilizes photon-assisted tunneling (cite alex ma and others). This method first starts from deep in a Mott-insulating regime where there is exactly an integer number of atoms per lattice site. Then a potential gradient is applied to the system such that increases the on-site potential energy by E Hz per site that is larger than the interaction energy U. Then the lattice

[§]This bound is determined by the Lieb-Robinson bound, which for a single-atom in a lattice is determined by the steepest slope (maximum group velocity) of its corresponding band.

depth is lowered to intermediate lattice depth $\approx 15E_r$ where the tunneling J is still much smaller than U or E. The lattice depth is then modulated at small amplitude at various frequencies to restore tunneling between the sites that are currently far away from resonance. When the frequency matches the energy difference between two sites, it restores tunneling and appears as fluctuations away from the Mott-insulating state.

There is a useful asymmetry in this protocol due to the on-site interactions. In the regime where $E > U$, the energy difference for an atom to hop to neighboring sites will cost either $E + U$ or $E - U$ energy depending on the direction of increasing gradient potential. This means that by measuring out both resonance conditions both E and U can be calibrated locally. This is demonstrated in Fig. 2.7 where the two resonances are measured, and the variance of the tilt E and the interaction U across the measured region reveal residual on-site disorder and on-site curvature.

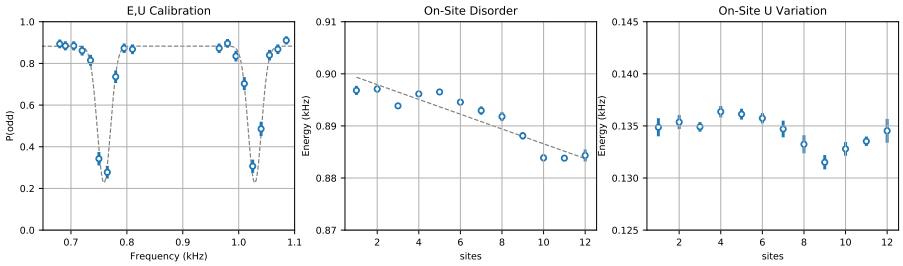

Figure 2.6: Calibrate Interaction and Tilt a, 2D **b,** Variation of tilt, curvature of offset, **c,** Variation of interaction, variation of on-site curvature

While the tilt E here is described as purely a part of a process that is necessary to suppress tunneling such that U and on-site differences can be measured, the tilt itself is also sometimes the quantity of interest. In some experimental schemes that implement synthetic magnetic fields in ultracold atom experiments, a potential gradient is used to suppress the bare, resonant tunneling in the lattice

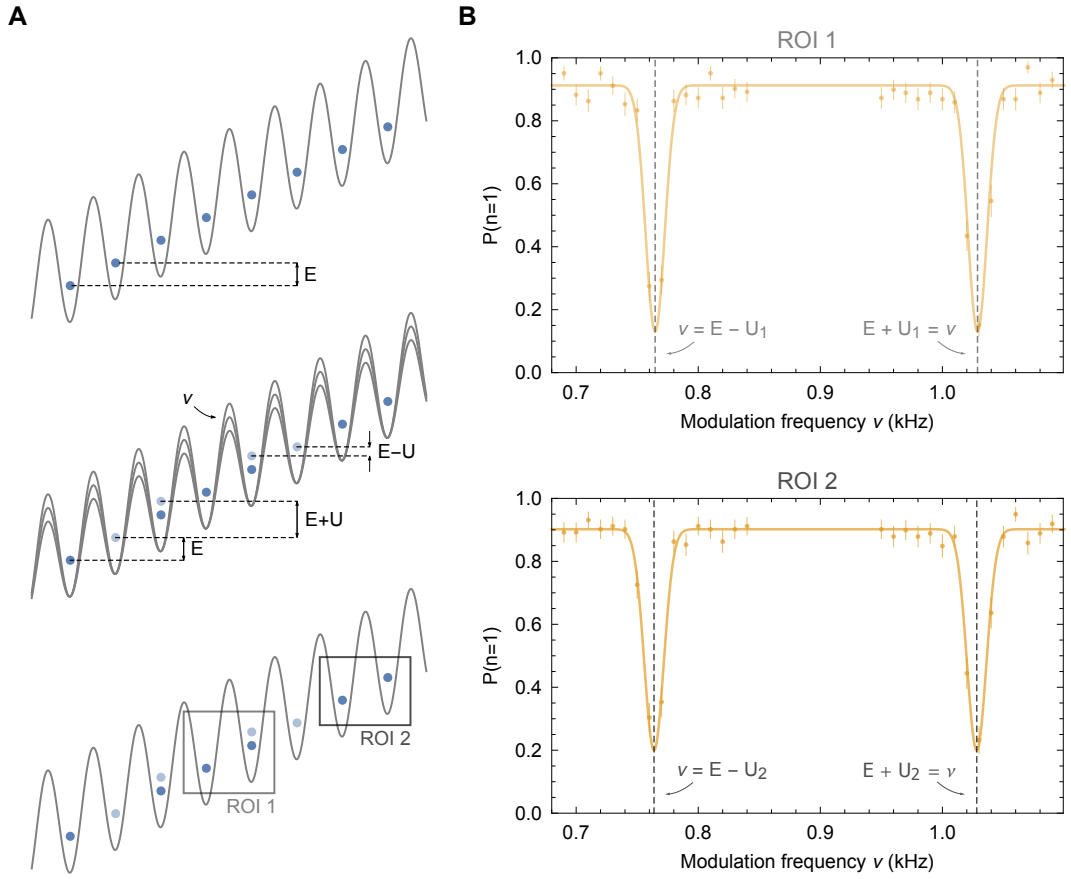

Figure 2.7: Calibrate Interaction and Tilt 2a, 2D **b,** COMBINE FIGURES

J along one direction which is then restored with a spatially varying phase. This has been explored in several cold atom experiments (cite bloch and ketterle people) and was implemented in this system to probe the Harper-Hofstadter model (cite erics paper) and is described in significant detail here (eric's thesis).

2.4.4 On-site Disorder pattern h_i : adiabatic transfer

The generation of single-site resolved potentials h_i are created via the DMD installed in the apparatus and are used extensively for state initialization and site-occupation read out during imaging. However, in both of these cases, the absolute depth of the potentials used is not particularly important since both procedures are relatively insensitive to them. However, some of the experiments in this thesis rely on a particular relationship of the on-site potential offsets h_i, to both the tunneling strength J and interaction strength U. By calibrating these potential offsets using the atoms we can both compare how precisely the DMD can produce a desired optical potential and the absolute height of these potential in Hz.

We used a similar protocol to the U calibration method mentioned above in §2.4.3 and is similar a hybrid of the protocols used in previous studies (cite photon assited tunneling and ising paper). The method starts with a unity-filled Mott-insulating state. A tilt of strength E Hz/site is then applied to the system to bring all sites far from resonance with their neighbors. The lattice depth is then reduced to an intermediate depth with appreciable but small tunneling. The additional potential pattern is then turned on approximately adiabatically with respect to only the nearest neighbor tunneling strength J. Since the potential that is applied has varying on-site potentials h_i, the resonsance condition is again re-established when the energy difference between neighboring sites, $\Delta_i = h_i - h_{i-1}$, compensates for the energy offset $E - U$. The signal is to then find when the average on-site occupation changes from $n = 1$ atom to $n = 0, 2$. This is actually measured in-situ as a change in parity. The example for this method shown in Fig. 2.8 is performed for an on-site po-

tential sampled from a quasi-periodic distribution: $h_i = W \cos(\beta 2\pi i + \phi_o)$, where β is the golden ratio ≈ 1.618, i is the site-index, and ϕ_o is an arbitrary phase factor.

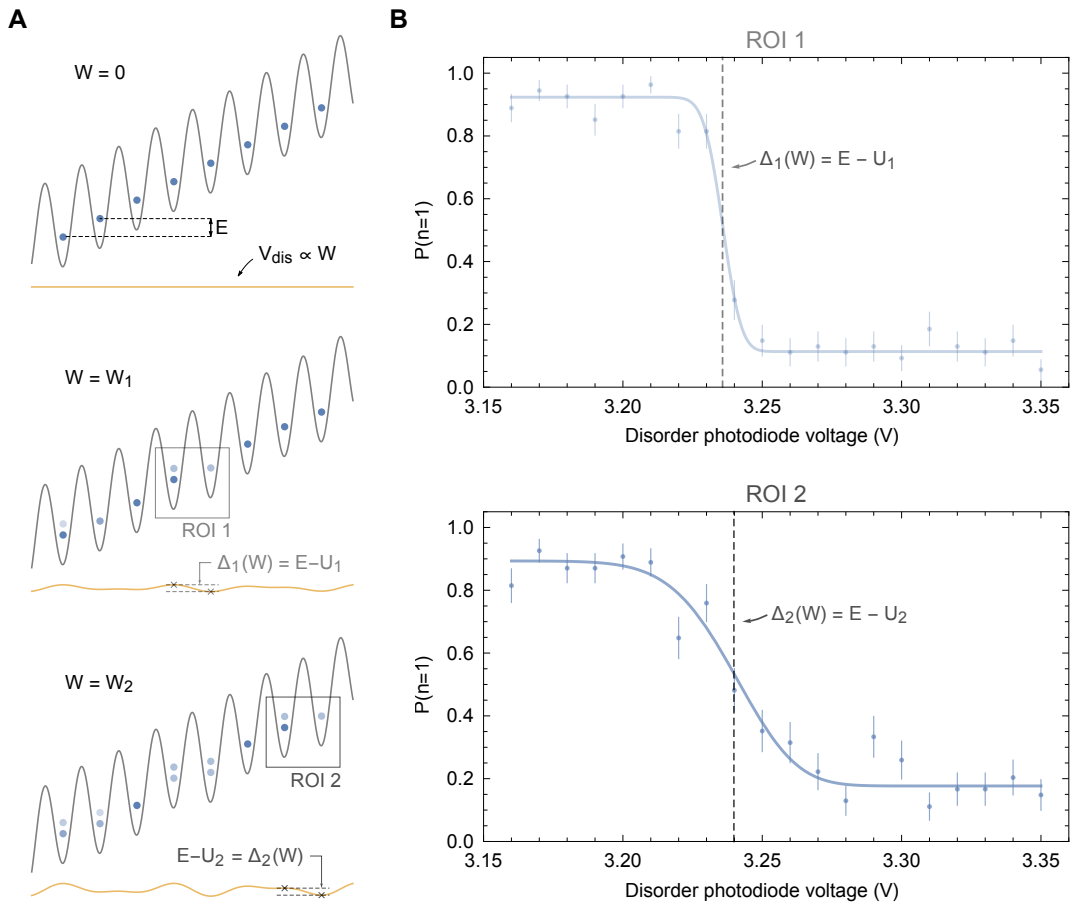

Figure 2.8: Calibrate Disorder .. on-sit epotential 2a, 2D **b,** COMBINE FIGURES

This protocol is also described in the supplementary of this paper (cite MBL).

2.4.5 Heating rates : spontaneous scattering

As discussed earlier in §2.1.3, the spontaneous scattering rate provides a limit on the lifetime of many-body coherent processes. To estimate this limit, we determine the contribution of the spontaneous scattering rates present from all the confining optical potentials in the system. The approximate background lifetime related to background collisions with hot atoms (this is related to the vacuum quality in the glass cell) is a lifetime of $\tau_{Bkg} = 33(3)$s or scattering rate $\gamma_{Bkg} = 0.03(3)$ Hz. By measuring the atom loss late from relatively weak traps as a function of optical potential depth, we can measure the contribution of the additional optical potential to heating and the offset that comes from background gas collisions. In general, this loss will follow an exponential form $\sim n(t) = N_o e^{-\gamma_{Bkg} t - \gamma_{Optical}(v) t}$. By holding the atoms in just an optical harmonic potential and the axial confinement lattice, we were able to find good agreement with the predicted spontaneous scattering rate and the approximate background collision rate estimated by previous works (Fig. 2.9).(cite theses). This measurements put an approximate single-atom lifetime for all experiments in this thesis to be $\tau_{comb.-ax} \approx 14$s in the axial-lattice configuration and $\tau_{comb.-big} \approx 19$s in the big-lattice configuration.

2.4.6 MI to SF heating? THINK ABOUT THIS LATER

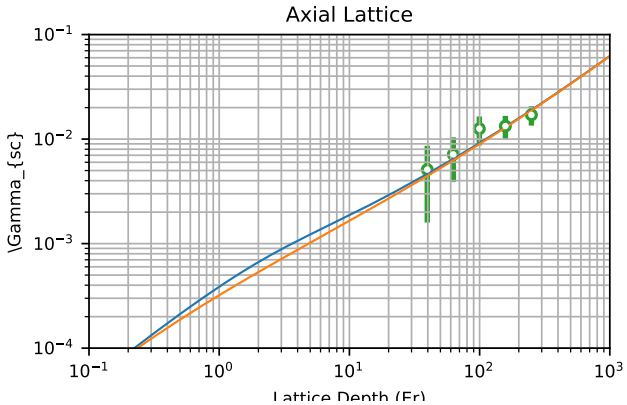

Figure 2.9: Axial Lattice Heating Rate a, ADD INSITU PICTURE TO MAKE IT CLEARER + EXP DECAY

3

Correlations, Entanglement, and Quantum Phase Transitions

Phase transitions, classical or quantum, are a celebrated paradigm in physics for describing the macroscopic properties of many-body systems independent of their microscopic parameters. These phases are described by a canonical diagram that distinguishes between an "ordered" and "disor-

dered" macroscopic phase of the system via a quasi-local observable known as an "order parameter". This parameter taking on some non-zero value in the "ordered" regime and becoming zero in the "disordered" regime. The transition of the macroscopic system from one phase to another happens as a function of the tuning of the equilibrium temperature of the system: the solid to liquid transition at the melting point, the ferromagnetic to paramagnetic transition at the Curie point, or the condensing of bosonic atoms into a Bose-Einstein condensate (BEC) at the critical temperature of a trapped, ultra-cold atomic gas (cite someone, probably subir). This transition occurs at a critical point of this tuning parameter between the two phases and describes where the order parameter becomes non-zero.

In classical systems, these thermodynamic transitions occur at a particular temperature because it is the relation of the energy of a microscopic parameter in the system to the average energy characterized by this temperature that governs the order of the system. Additionally, the ability of the system to actually change its macroscopic ordering requires that the system possesses microscopic fluctuations, in this case driven by the microscopic fluctuations that accompany a given temperature. The ability of these fluctuations to drive the system from a disordered state towards an ordered one requires, as the name would suggest, the correlation of these fluctuations across the system such that they bring the system collectively towards a macroscopically ordered state. As such, a length scale can be defined that associates the spatial extent of these correlations in the system and gives rise to many of the characteristic associations with phase transitions such as the correlation length diverging at the critical point.

The most remarkable aspect of this entire phase transition paradigm being that these qualitative

behaviors depend only up on a few macroscopic parameters such as dimensionality or underlying symmetries in the system. This means that given some appropriate rescaling of different systems, their behavior will be identical and therefore the behavior of the transition is actual "universal".

Many of these concepts (but not all) from classical phase transitions an be related as well to quantum phase transitions. The study of quantum phase transitions involves the tuning of a coupling parameter in a Hamiltonian between two non-commuting terms as schematically shown in:

$$H = H_o + gH_1 \tag{3.1}$$

where $[H_o, H_1] \neq 0$. The transition of this system occurs at a critical coupling point g_c and is only considered at equilibrium which can occur even when $T = 0$. * Fundamentally, the system still needs fluctuations even at $T = 0$ to allow for the macroscopic ordering at the phase transition. The difference being that these fluctuations are now driven as purely "quantum" fluctuations that persist even at $T = 0$ due to the Heisenberg uncertainty principle. These quantum fluctuations also lead to a divergence in a correlation length across the system at the critical point. The question that then naturally arises is "how much are these correlations purely quantum?" This notion of uniquely quantum correlations is intimately related to the concept of entanglement in quantum systems – perhaps the most celebrated hallmark of "quantum-ness." In some cases, the entropy induced in a system due to it's entanglement has been used to distinguish the uniquely quantum aspect of these phase transitions. Scaling behavior of these quantities at the critical point help distinguish the

*It is at this point, the assumption of a system at equilibrium and $T = 0$, that all quantum phase transitions are typically assumed to refer to the transition in the ground state properties.

system's universality class. Analytical and numerical results for this entanglement behavior has been studied theoretically for both spin systems (Ising and Heisenberg models) and itinerant particle, lattice models (bosonic and fermionic particles). (philipp ref 22 and 26).

This mapping of the language and Landau-Ginzburg framework of phase transitions, however, does not apply ubiquitously to all quantum phase transitions. Notably, in the case of fractional quantum hall states (cite from philipp's thesis) or spin liquids (cite from philipp's thesis) their isn't a clear notion of a local order parameters that distinguishes these phases, but rather their non-local entanglement that captures their behavior.

This section will start of with some generic discussion about correlations and entanglement in quantum systems. The presence of such correlations and their relation to quantum phase transitions will be discussed in the context of experiments measuring such correlations for the superfluid to Mott-insulating transition and the Ising paramagnetic to ferromagnetic transition, both experimentally realized in 1D.

3.1 Correlations and Entanglement

Entanglement is one of the most counterintuitive and truly unique (results/outcomes) of quantum mechanics. It was famously shown by Bell that entangled quantum particles can exhibit correlations that are stronger than physically possible in classical, local theories (cite Bell). † These highly

†In fact, a very common question typically asked of any result from a quantum simulation experiment is how "quantum" are the results. As in, how uniquely can the observed behavior be attributed to the system being a quantum one and not just one, for example, described by a wave theory. The violation of Bell's inequality by a system is one of these few cases that is simply impossible in classical, local theories.

entangled quantum states that exhibit such classically violating correlations are known as Bell states and have been verified experimentally (cite aspect and recent loop-hole free version) and rule out proposed "hidden variable" theories – powerfully confirming that quantum mechanics as a correct description of nature.

Correlations and the presence of entanglement in a quantum system are often considered to be synonymous. For the purpose of clarity, this thesis will describe entanglement as a qualitative descriptor a

Correlations, Entanglement, Entropy, and Mutual Information

footnote about physics correlations and statistical correlations

3.1.1 Some comments near a phase transition

General statements that at a phase transition your correlation length diverges. This, somewhat, implies the states entanglement entropy also, indeed, increases.

3.2 Superfluid to Mott-insulator transition

The SF to MI transition doesn't seem to have this. But why?! Well, it seems it has to do with the fact that the correlations in the ground state are really quite small. In our case, it is completely swamped by the correlations that arise from a conservation rule in our systme

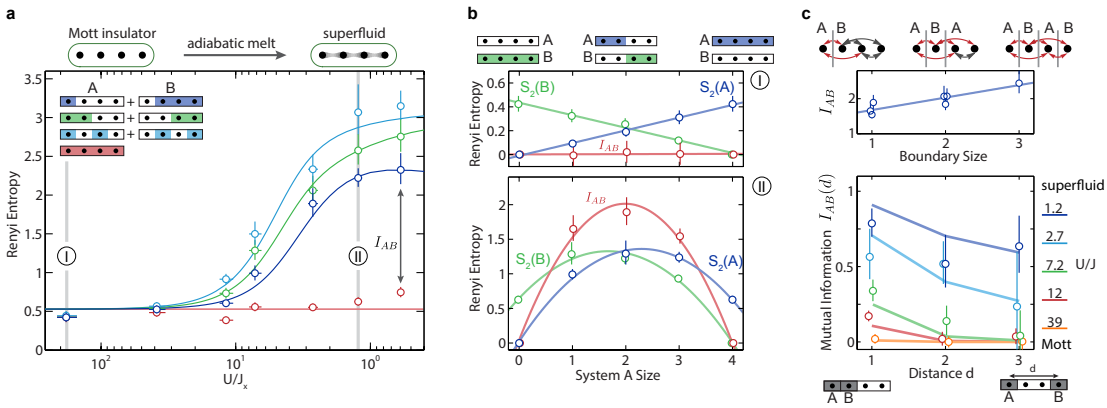

Figure 3.1: Measured Entropy in the MI to SF transition,

3.3 Ising model phase transition

This section will start with a brief overview of another canonical phase transition in the Ising model with both longitudinal and transverse magnetic fields. Importantly, the implementation of this model in our Bose-hubbard model will have behavior that is more akin to the celebrated phase transition behavior expected without any conservation rules for equilibrium systems. Through the use of our DMD, we can access the full-counting statistics of the quantum state in the Fock basis. This allows us to directly probe the order parameter of the quantum phase, the single-site entropy, and the reversibility of the transition which probes its overall purity.

This model has been previously realized in this same experimental apparatus (cite paper) and is more thoroughly discussed in the following theses (cite waseem and alex ma). The mapping from the Bose-hubbard model to a spin model was first proposed by Sachdev et. al (cite sachdev) and is accomplished my working in a reduced Hilbert space via a strong potential gradient in the optical lattice. The primary ingredients of this mapping are shown in Fig. ??.

This mapping starts in a regime where $U \gg J$ and $U/2 < E < U$[‡]. This realizes a set of eigenstates that are approximately described by the Fock basis. The gradient potential, E, is then increased till $E > U$. This ramp will have brought site on-resonance with its neighbor. However, the celebrated dynamics of this transition arise from the collusion of all the particles in the system such that they transfer in a many-body coherent way.

$\tilde{t} = t/J$

$h_x = 2^{3/2}\tilde{t}$

$h_z = 1 - \tilde{\Delta}$

$D\tilde{e}lta = \Delta/J$

$\Delta = E - U$

$\delta_z^i = \delta E_i/J$

Transition happens at $E = U + 1.85t$ or $h_z = 1 - 0.66h_x$

$$H = J\sum_i S_z^i S_z^{i+1} - (h_z + \delta_z^i)S_z^i - h_x S_x^i \tag{3.2}$$

(we also get this same conservation rule but it arises as some sort of frustration in the ground state on the AFM side)

[‡]The lower bound forgoes the contribution of second-order hopping processes that incorporate states outside of the prescribed basis for a faithful mapping to the Ising model. This was found to be a necessary step since these second-order processes provided a non-negligible fraction of population evolved into these states.

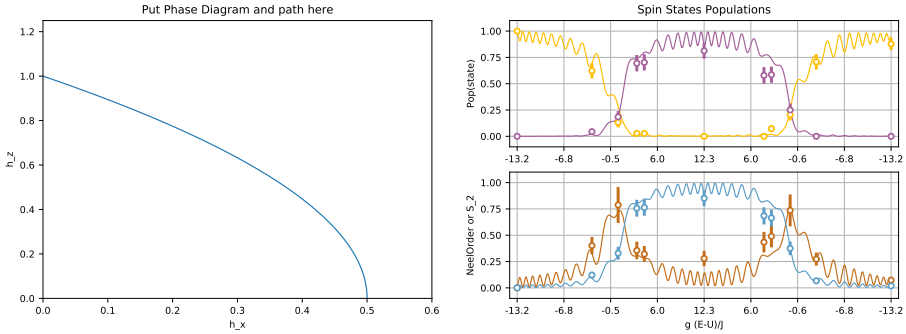

Figure 3.2: Measured Entropy in the MI to SF transition,

4

Isolated quantum systems and the transition to thermal subsystems

What about if we go away from equilibrium? Really this is a much vaster world when we don't restrict ourselves to just ground states.

Mostly just go through adam's paper here. Briefly describe the universe in a box and statistical

mechanics perhaps

4.1 A new kind of phase transition

4.2 Thermalization

5

Adding integrability back with many-body localization

Go through the usual run around of doing anderson localization to break transport in the system, then talk about interacting systems, then many-body localization.

Split up of Sp+sn if we haven't arleady done that (which we probably will have). Then just de-

scribe what you hope to see see in the system and our plots and correlator

5.1 Breaking Integrability with Localization

5.2 Anderson Localization

5.3 Aubry-Andre Localization

5.4 Many-Body Localization

5.5 Types of correlations and Entanglement

6

Critical Dynamics of MBL

All critical data. Correlation distance, Slow grwoth (subdiffusive) High order correlations (refer to appendix for stirling numbers, memoization implementation), growth in time?

6.1 Anomalous Diffusive Transport

6.2 Determining Critical Thermalization

6.3 Correlation Structure

6.4 High-order Correlations

6.5 Hamming distance?

7

Contact with a thermal bath

8

Conclusion

What is our outlook? MBL with other degrees of freedom? Spins? different disorder types? Larger systems? driven systems?

quasi-crystaline> FQH-CMI stuff?

2D arrays (efi and dom)

random unitaries

A

Atomic Properties of Rb^{87}

Add the usual atomic properties here

someone

B

Numerics

All python and matlab scripts can be found at gitHub::mnrispoli

someone

C

Chapter 1 Calculations

Starting from two propagating plane waves, we can find the shape of the potential that is proportional to the intensity:

$$V_{Latt} \propto |e^{i(k_l x - \omega t)} + e^{i(k_l x + \omega t)}|^2 \propto \cos^2(k_l x) \propto \cos(2k_l x) \tag{C.1}$$

Note, that we have left the potential as a function of the laser wavevector. This is important for

the definition of the "recoil energy" of the lattice. To simplify calculations, we subtract off the mean energy of the lattice such that it has an amplitude V_o which we define as the lattice depth.

$$V_{Latt} = \frac{-Vo}{2} \cos\left(2k_l x\right) \tag{C.2}$$

Band Structure Calculation (more explicit)

Wannier functions and fourier components

Approximations for gaps for shallow lattice and deep lattices

Deviation of Wannier function from gaussian

Mean Field Phase Diagram

someone

D

Chapter 2 Calculations

Calculations for fresnel coefficients versus angle

Calculations for Disorder and zero-point energy

Calculations for heating rates

References

[1] Eigen, M. (1971). Selforganization of matter and the evolution of biological macromolecules. *Naturwissenschaften*, 58(10), 465–523.

[2] Knuth, D. E. (1968). Semantics of context-free languages. *Mathematical Systems Theory*, 2(2), 127–145.

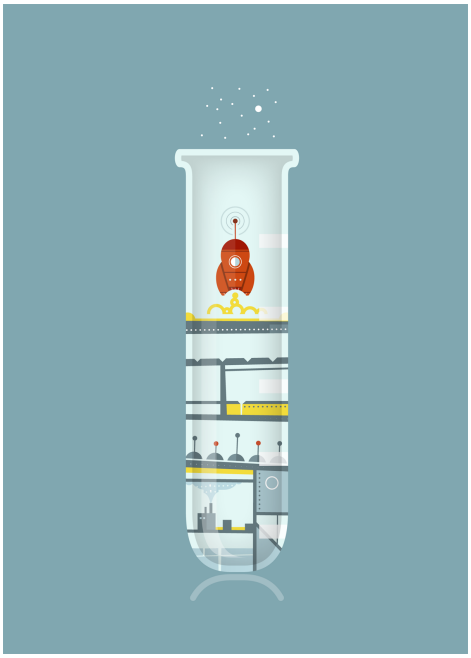

This thesis was typeset using LaTeX, originally developed by Leslie Lamport and based on Donald Knuth's TeX. The body text is set in 11 point Egenolff-Berner Garamond, a revival of Claude Garamont's humanist typeface. The above illustration, *Science Experiment 02*, was created by Ben Schlitter and released under CC BY-NC-ND 3.0. A template that can be used to format a PhD dissertation with this look & feel has been released under the permissive AGPL license, and can be found online at github.com/suchow/Dissertate or from its lead author, Jordan Suchow, at suchow@post.harvard.edu.